

Article

Numerical Study of the Winter–Kennedy Flow Measurement Method in Transient Flows

Binaya Baidar ^{1,*}, Jonathan Nicolle ², Bhupendra K. Gandhi ³ and Michel J. Cervantes ¹

¹ Division of Fluid and Experimental Mechanics, Luleå University of Technology, SE-97187 Luleå, Sweden; michel.cervantes@ltu.se

² Institut de recherche d'Hydro-Québec (IREQ), Varennes, QC J3X 1S1, Canada; nicolle.jonathan@ireq.ca

³ Department of Mechanical and Industrial Engineering, Indian Institute of Technology, Roorkee, Uttarakhand 247667, India; bkgmefme@iitr.ac.in

* Correspondence: binaya.baidar@ltu.se; Tel.: +46-920-493895

Received: 6 February 2020; Accepted: 8 March 2020; Published: 11 March 2020



Abstract: This paper explores the possibility of using the Winter–Kennedy (WK) method for transient flow rate measurement in hydraulic turbines. Computational fluid dynamic (CFD) analysis of a numerical model of an axial turbine was carried out for accelerating and decelerating flows. Those were obtained by linearly opening and closing of the guide vanes, respectively, while retaining the inlet pressure constant during the simulations. The behavior of several WK configurations on a cross-sectional plane and along the azimuthal direction of the spiral casing was studied during the transients. The study showed that there are certain WK configurations that are more stable than others. The physical mechanism behind the stability (or instability) of the WK method during transients is presented. Using the steady WK coefficient obtained at the best efficiency point (BEP), the WK method could estimate the transient flow rate with a deviation of about 7.5% and 3.5%, for accelerating and decelerating flow, respectively.

Keywords: Winter–Kennedy; flow rate; transient flow; hydropower; CFD

1. Introduction

The integration of intermittent renewable energy sources like solar and wind into the grid results in grid fluctuations. The grid fluctuations are usually stabilized by hydropower plants. Thus, hydropower will likely remain a key link to ease the integration of different renewable energy sources within the grid in the coming decades [1,2]. This demands the highly flexible operation of the hydropower plants. Consequently, the plants undergo frequent transient events such as start–stops and large ramping rates. Most research is focused on the hydro-mechanical aspects of the transients [1], variable-speed operation [3] and designing flexible hydraulic turbines to support flexible operations [2]. Besides, the instantaneous flow rate in the transients is a key parameter to study the hydro-mechanical effects on the turbine components or to quantify the total volume of water flow during such events. Thus, the accurate transient flow rate measurement in a hydraulic turbine has become a necessity.

It is still challenging to accurately measure the transient flow rate in practical engineering applications, such as in hydraulic turbines. There is no standard method to measure transient flow rate in a hydraulic turbine: there are only methods to measure the steady flow rate (see IEC 60193 [4] for model testing or IEC 60041 [5] and ASME PTC-18 [6] for field testing). Most of the methods described in these standards are applicable to high-head turbines. Similar measurement in low head turbines is challenging, as the intake for such plants is usually short and has continuously varying cross-section. Some recent advancements in the acoustic transit-time method showed a promising result, with a deviation of less than 0.2% from a code-accepted reference flow meter [7]. In this study, the authors

employed pairs of ultrasonic transducers installed in a non-uniform transition section at the intake. Yet, the ultrasonic measurement method may be expensive and time-consuming [8].

There have been substantial studies in transient flow rate measurements, mainly in pulsating flows with several techniques. Leontidis et al. [9] developed an ultrasonic flowmeter for measuring flow rate fluctuations in cryogenic conditions. Cheesewright et al. [10] presented a Coriolis flowmeter with a high dynamic performance in pulsating flows is presented by an electromagnetic flowmeter was developed to measure transient flow by Lefebvre and Durgin [11]. However, these transient flowmeters are applicable to a laboratory or simple engineering applications. For a hydraulic turbine, the transient flow rate in a laboratory, i.e., model testing, may be measured by recording the water level variation over time in the upstream tank with a controlled free surface (see the experimental work by Fraser et al. [12]). However, the usual choice in model testing remains an electromagnetic flowmeter [13,14]. These flowmeters may not provide accurate instantaneous results as they have a time response of 0.5 s or above. Furthermore, the utilization of these techniques in field testing of hydraulic turbines can be infeasible or expensive.

Transient flows have been extensively studied in straight pipes [15–17] and channels [18–20]. From these studies, three main stages in flow acceleration have been identified. The first stage is a frozen stage where the turbulent shear stress largely remains unchanged, so the mean flow field evolves like in a laminar flow. Inertia dominates and the flow responds to the imposed pressure gradient. There is a rapid response of the turbulence and gradually exceeds the influence of inertia in the second stage. The third stage is a quasi-steady stage where the turbulence and the mean flow field converge towards their steady distributions based on the final Reynolds number. Consequently, the wall-shear stress in ramp-up flow is larger than the quasi-steady value initially and becomes smaller in the initial stage before approaching the quasi-steady value. In ramp-down flows, the wall-shear stress may be either larger or smaller than the corresponding quasi-steady values in flow deceleration depending on how strong the deceleration is [21]. Seddighi et al. [19] showed through a direct numerical simulation (DNS) study of channel flows that in strongly decelerated flow, the wall-shear stress is smaller initially and then becomes larger than the quasi-steady values. Furthermore, the flow and turbulence quantities are significantly different from the corresponding quasi-steady value in the ramp-up flow whereas much less in ramp-down flow. Accelerating and decelerating flows are two increasingly occurring transient flows in hydraulic turbines due to frequent ramp-up and ramp-down of the machine. Therefore, a better understanding of the transients has also become a necessity for accurate transient flow rate measurement.

One of the popular methods to measure the relative flow rate in low head plants during steady operation is the Winter–Kennedy (WK) method. The WK method is based on a simple radial equilibrium flow assumption, i.e., a balance between the radial pressure gradient and centrifugal forces. The method was first described by Winter and Kennedy almost a century ago [22]. It utilizes a pair of differential pressure taps placed at a section of the spiral casing (SC) to measure the pressure difference ΔP . ΔP is then used to calculate the flow rate (Q), such as:

$$Q = K_{WK} \Delta P^n, \quad (1)$$

where K_{WK} is the flow coefficient called the WK constant/coefficient and n is an exponent. K_{WK} and n values are usually calibrated using model test results or a previous efficiency test result. The value of n ranges from 0.48 to 0.52 [5] but is usually kept at 0.5. The uncertainty in the measurement can range up to 2% under similar conditions [23,24].

The WK method has some cost advantages and is easy to implement. It is widely used in relative efficiency measurements, or to find an optimum cam relationship in double regulated machines. Another benefit of the WK method is that the ΔP is measured continuously thus providing a possibility of using WK as a transient flow rate measurement method.

Therefore, the present work explores the possibility of using the WK method in transient flows. For this purpose, a numerical model of a low head Kaplan model turbine has been developed and the

computational fluid dynamics (CFD) simulations using unsteady Reynolds-averaged Navier–Stokes (URANS) equations have been carried out. A previous study by the authors presented in [25] showed that there could be appropriate locations and configurations of the stable WK pressure taps in decelerating flow. Therefore, the present study is conducted considering several feasible locations for the WK measurements in decelerating, as well as in accelerating flows. The WK coefficients in the transient flows are compared to the coefficients obtained at steady flow conditions. The behavior of the WK configurations in the transient flows is studied in detail.

In this paper, the test case considered is described initially, then the numerical modeling and simulation approach to achieve the transient flows are described. The method section describes the WK configurations considered. The result section presents the flow rate and the pressure difference variation with time and the behavior of the WK coefficients during the transients. The performance of the WK method is compared with the GV opening flow rate estimation approach. Finally, the flow physics during transients, along with steady operations, are presented in the paper.

2. Methods

2.1. Porjus U9 Model Test Case and the Computational Domain

The test case of the present study is the Porjus U9 model turbine, which is a 1:3.1 scaled model of the actual hydropower plant located in Sweden. The model turbine consists of a penstock, an SC, a distributor with 18 stay vanes (SVs) and 20 guide vanes (GVs), a Kaplan runner with six blades, and an elbow-type draft tube. The flow rate at the best efficient point (BEP), Q_{BEP} , is $0.71 \text{ m}^3/\text{s}$ at the GV angle (GVA, α) of 26.5° . The model turbine with the test rig is shown in Figure 1a. The computational domain for the present study includes the penstock, SC and distributor. More details on the Porjus U9 model turbine may be found in [26]. Furthermore, previously conducted experiments using laser Doppler anemometry (LDA) at the inlet of the SC by Amiri et al. [26] and a separate study conducted by Mulu and Cervantes [27] at two locations in the SC were used to validate the numerical model; see Figure 1b for the measurement locations in the experiment conducted by Mulu and Cervantes.

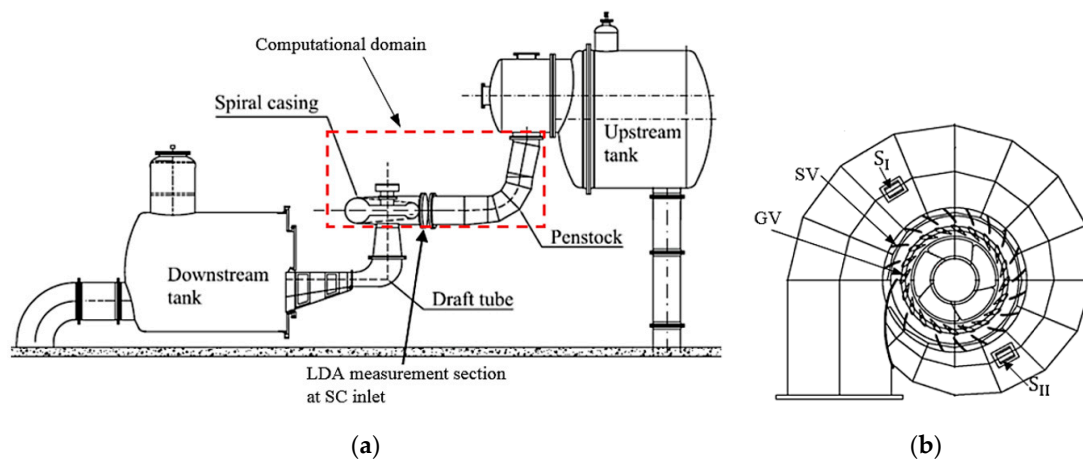


Figure 1. (a) Porjus U9 test rig facility with the computational domain marked by the dashed-rectangle; (b) top view of the turbine with laser Doppler anemometry (LDA) measurement locations: S_I and S_{II} from Mulu and Cervantes [27].

2.2. Transient Cases

The present study considers accelerating and decelerating ramp-type flows, which were obtained by linearly opening and closing the GVs in the numerical simulations, respectively. For both cases, the GVs movement was set to the rotational speed (ω_{GV}) of about $8.83^\circ/\text{s}$ of the GV angle. The GVs were opened from $\alpha = 2^\circ$ to 26.5° (BEP) during acceleration and closed from $\alpha = 26.5^\circ$ to 2° during deceleration. These simulations were representative of a rapid ramp-up and rapid shutdown condition.

Note that there is no runner in the study and hence only the GVs are moved (rotated) to obtain the transient flows, so it is representative of an axial turbine. A minimum α of 2° was chosen mainly for three reasons: a) to avoid water hammer effects, b) mesh constraints, and c) the necessity of having a minimum flow rate during simulations.

The transient times in the acceleration and deceleration cases are denoted by t_a and t_d , respectively. These times are presented in reference to the time when the transient starts. As the GVs rotational speed was $8.83^\circ/\text{s}$ of the GV angle and the range of GVA movement was 24.5° , the total ramp time for both cases was $\cong 2.77$ s. Before starting the transients, the steady simulations were run for a sufficiently long period of time at a constant α , i.e., at $\alpha_{\text{initial}} = 2^\circ$ for the acceleration case and $\alpha_{\text{initial}} = 26.5^\circ$ for the deceleration one. Furthermore, steady flows were obtained at stationary GVs opening with an angle of 26.5° , 18° , 13° , 8° , and 4° , for comparison with the transient results. Table 1 shows a summary of the transient cases.

Table 1. Transient cases.

Case	$\alpha_{\text{initial}} (^\circ)$	$\alpha_{\text{final}} (^\circ)$	Ramp Time (s)
Acceleration (GV opening)	2	26.5	2.77
Deceleration (GV closing)	26.5	2	2.77

2.3. WK Configurations and Locations

The WK configurations considered in this study are shown in Figure 2. Four cross-sectional planes along the SC's azimuthal direction: $\theta = 60^\circ, 75^\circ, 101^\circ$, and 124° were considered; see Figure 2a. At each cross-sectional plane θ , there were four WK configurations - two WKs in the upper half (WK_{1u} and WK_{2u}) and their mirrored configurations in the lower half (WK_{1d} and WK_{2d}); see Figure 2b. The WK coefficients K_{WKs} were calculated from Equation (1) considering $n = 0.5$ and ΔP as the difference in pressure between the outer and inner pressure points for a configuration: $\Delta P_{1u} = P_{ou} - P_{1u}$, $\Delta P_{2u} = P_{ou} - P_{2u}$, $\Delta P_{1d} = P_{od} - P_{1d}$, and $\Delta P_{2d} = P_{od} - P_{2d}$. As some spiral model turbine casings are manufactured in two blocks with a horizontal interface in the middle of the guide vanes, the outer pressure taps, P_{ou} and P_{od} , are considered above and below this interface to avoid the connecting plane, $\beta = 0^\circ$ shown in Figure 2b. The choice of these WK configurations is to cover feasible measurement locations of the WK pressure taps in the SC, to understand the stability of the WKs along the azimuthal direction of the SC and the choice of the pressure taps' locations at a cross-sectional plane.

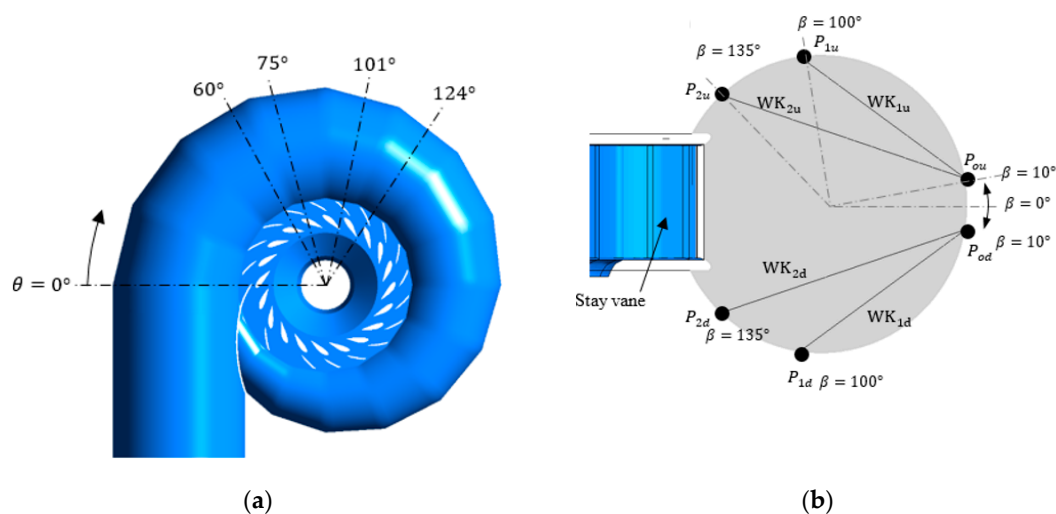


Figure 2. (a) Locations of the Winter–Kennedy (WK) configurations at four cross-sections along the azimuthal direction of the SC at $\theta = 60^\circ, 75^\circ, 101^\circ$, and 124° ; (b) WK pressure points marked with the black circles and combinations represented by the solid lines for each cross-sectional plane. The angular locations of the pressure points on the plane are given by β angles, which are referenced from $\beta = 0^\circ$.

2.4. Numerical Approach

2.4.1. Computational Domain

The computational domain is shown in Figure 3a. It encompasses penstock, SC, and distributor consisting of SVs and GVs. All the domains were composed of structured hexahedral meshes created using the software ICEM CFD; see representative meshes in the penstock and the SC in Figure 3b,c. A general grid interface (GGI) was used to connect the domains. The mesh for the distributor was created for a single passage containing a GV and an SV and then copied and rotated to create the distributor. This ensures the one-to-one mesh connection at the interfaces of the two adjacent passages and makes GVs movement possible. Since there are only 18 SVs in the distributor, two passages were without SVs (see Figure 2a).

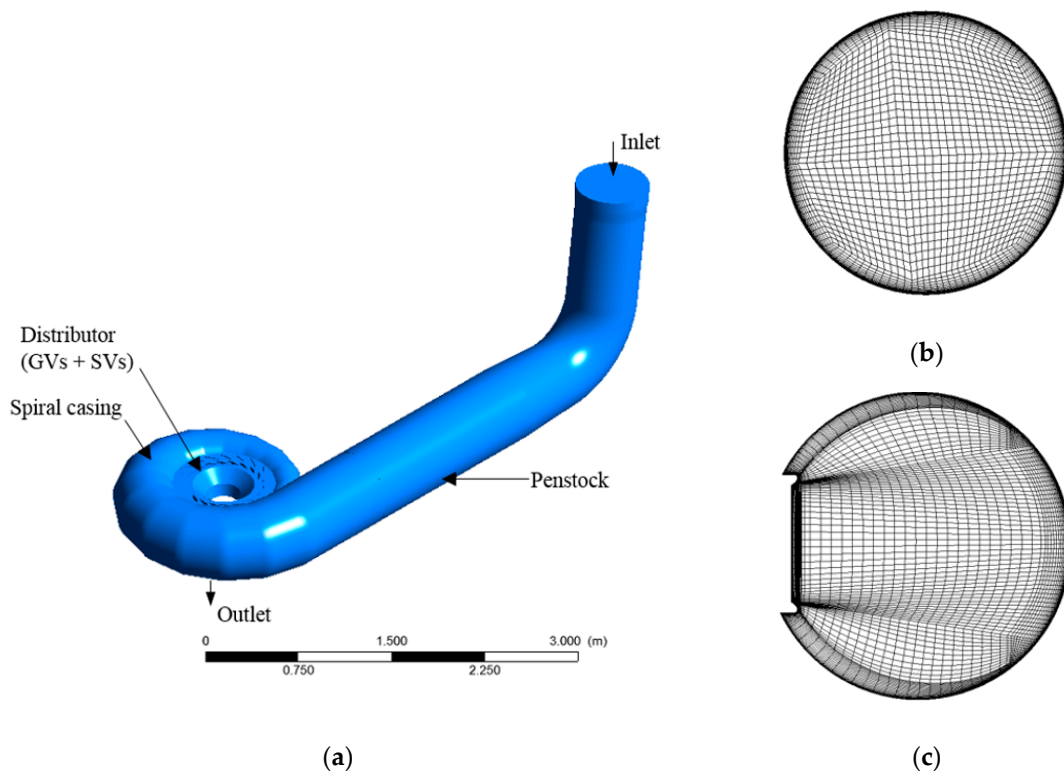


Figure 3. (a) Computational domain; (b) mesh at a section of the penstock; (c) mesh at a section of the SC.

2.4.2. Guide Vanes Motion

In order to mimic the GVs motion in the simulations, either mesh deformation [28] or re-meshing techniques [29] are usually employed. In this study, the mesh deformation technique was used to rotate the GVs. The mesh motion model used is based on the displacement diffusion equation, $\nabla \cdot (\Gamma_{disp} \nabla \delta) = 0$; where Γ_{disp} is the mesh stiffness and δ is the displacement relative to the previous mesh locations. The mesh stiffness increases exponentially as the control volume size decreases to keep the cells in the boundary layer mostly unchanged. This equation is solved at the start of each time step. With this model, the displacements applied on boundaries are diffused to other mesh points preserving the relative mesh distribution of the initial mesh. More details on this mesh deformation model may be found in the software's solver guide [30].

The transient simulations were conducted with two intermediate meshes at $\alpha = 18^\circ$ and 8° to conserve the quality of the mesh. The transient simulations were performed considering a small GV angle overlap between two consecutive simulations. As a matter of fact, a small bump in the variables was observed at the start of the intermediate meshes and the overlapping zones were removed during

post-processing for smooth results. This method did not affect the overall solution, as the solution of the second mesh followed (overlapped) the solution of the previous mesh. The GVs were rotated around their respective rotational axes. Representative meshes around the GVs at different time instants during the deceleration are shown in Figure 4.

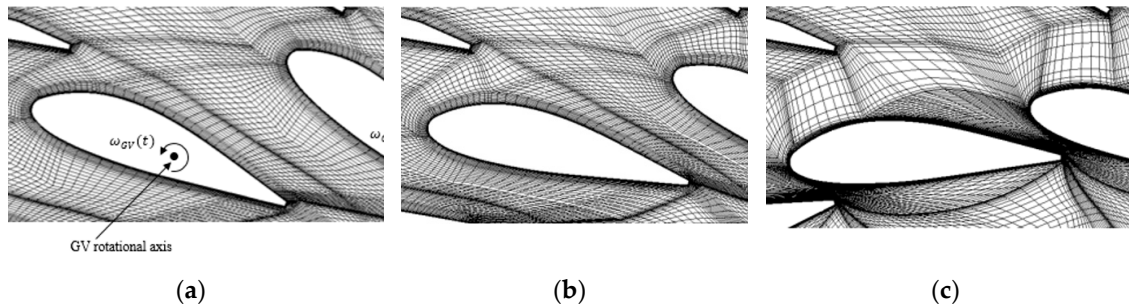


Figure 4. Guide vanes (GVs) meshes at different time instants during a closure. (a) $t_d = 0$ s; (b) $t_d = 1$ s; (c) $t_d = 2.5$ s.

2.4.3. Governing Equations and Boundary Conditions

All the simulations were performed using the software ANSYS CFX v19.1. The flow was modeled using unsteady Reynolds-averaged Navier–Stokes (URANS) equations. The continuity and momentum equations can be expressed as:

$$\frac{\partial \bar{u}_i}{\partial x_i} = 0 \quad (2)$$

$$\frac{\partial \bar{u}_i}{\partial t} + \bar{u}_j \frac{\partial \bar{u}_i}{\partial x_j} = -\frac{1}{\rho} \frac{\partial \bar{p}}{\partial x_i} + \nu \frac{\partial^2 \bar{u}_i}{\partial x_j^2} - \frac{\partial (\overline{u'_i u'_j})}{\partial x_j} \quad (3)$$

where \bar{u}_i is a time-averaged velocity component, \bar{p} is the time-averaged pressure, ν is the fluid kinematic viscosity, and u'_i represents the fluctuating velocity component. The Reynolds stress term $-\overline{u'_i u'_j}$ is modeled with a turbulence model. The governing equations are discretized using the element-based finite volume technique implemented in the software. The High-Resolution scheme was used to discretize the advection term, which uses a special nonlinear technique to blend first to second-order schemes depending on the location solution field. The transient term was discretized with the second-order backward Euler scheme, as this scheme is robust, implicit, conservative in time, and does not have a time step size limitation, refer CFX solver guide for more information on the scheme [30]. Menter's $k - \omega$ SST (shear stress transport) model [31] was used to model turbulence. This turbulence model has shown satisfactory results in terms of robustness, stability, and accuracy in several previous hydraulic turbine studies [28,32–34] and transient flow simulations in pipes [35,36]. The automatic near-wall treatment developed by CFX was employed, which automatically switches from a low-Re formulation to wall-functions when the grid is not refined enough near the wall [30].

Water at 20 °C was considered as the working fluid, with no compressibility effects. The inlet boundary condition was a total pressure with a normal velocity profile (plug flow) at the inlet of the penstock with medium turbulence (5% intensity). The distributor outlet was defined as an opening boundary with a relative pressure. With these boundary conditions, the motion of the GVs induces the flow rate variation during the simulations. All walls were assumed smooth and no-slip boundary condition. The same set of boundary conditions was considered for all the simulations in this study.

2.4.4. Mesh Information and Numerical Uncertainties

Three different sets of meshes with a total number of elements: $N_1 = 9.75$, $N_2 = 5.45$, and $N_3 = 2.77$ million were used to study the uncertainty in the chosen mesh. For this, the grid convergence index (GCI) study was considered, following the guidelines provided in [37]. The study was performed at

the BEP flow condition with the time step $\Delta t = 0.0226$ s; the time step study will be discussed later. Table 2 presents the discretization uncertainty for the WK configurations at $\theta = 101^\circ$. In the table, ϕ_{ext}^{21} is the extrapolated value of the WK coefficients from N_2 mesh to N_1 mesh and $GCI_{fine\ mesh}^{21}$ is the uncertainty in the chosen mesh (N_1 mesh) in this study.

Table 2. Discretization uncertainty study using Richardson extrapolation following Reference [37]. ϕ_1 , ϕ_2 , and ϕ_3 are the WK coefficients obtained with N_1 , N_2 , and N_3 mesh, respectively.

Parameter	$\phi=K_{WK1u}$	$\phi=K_{WK1d}$	$\phi=K_{WK2u}$	$\phi=K_{WK2d}$
ϕ_1	0.0199	0.0170	0.0143	0.0127
ϕ_2	0.0196	0.0172	0.0143	0.0125
ϕ_3	0.0204	0.0181	0.0145	0.0128
ϕ_{ext}^{21}	0.0202	0.0168	0.0143	0.0129
$GCI_{fine\ mesh}^{21}$	1.4%	1.0%	0.1%	1.5%

Furthermore, the discretization uncertainty in the velocity along a vertical line at the inlet of the SC is presented for the chosen mesh in Section 2.4.5. The mesh information for the chosen set of mesh is summarized in Table 3. The mesh quality fulfills the minimum quality criteria required by the solver. Moreover, the mesh was chosen to maintain the good quality during the GV's movement.

Table 3. Mesh information for the chosen mesh set.

Parameters	Penstock	Spiral Casing	Distributor (SV + GV)		
			$\alpha = 26.5^\circ$	$\alpha = 18^\circ$	$\alpha = 8^\circ$
Total elements, in million	1.4	1.8	6.4	6.4	6.4
Max. element aspect ratio	9200	2429	416	516	557
Orthogonality angle, $^\circ$ (min, avg)	35, 84	19, 65	22, 59	19, 57	19, 56
y^+ (avg, max)	1, 495	20, 130	19, 224	16, 161	13, 67

The effect of time step size was conducted for the decelerating flow with the chosen mesh. Two time steps: $\Delta t = 0.0226$ s and 0.0057 s were considered, which corresponds to the GV rotational speed $\Delta\alpha$ of 0.2° and 0.05° , respectively. The maximum deviation in the transient flow rates obtained with these time steps was about 1.2% at $t_d \cong 1.42$ s. The variation of ΔP with time during the deceleration obtained from these time steps also showed similar results and the effect of the time step is negligible, further discussion about this is also presented in Section 3.1. All the simulations, transient and steady cases, were therefore conducted with the time step $\Delta t = 0.0226$ s. The simulations were carried out using distributed-parallel computation across two machines, each with 64 GB memory and 24 cores. The computers took a time period of about 6 days to complete each transient case simulation.

2.4.5. Validation Studies

The streamwise velocity distribution along a vertical line, Line A, at the inlet of the SC obtained from the chosen mesh solution is compared with experimental results in Figure 5. The velocities are scaled by the bulk velocity, U_b , calculated as the ratio of the BEP flow rate to the inlet area of the SC (Q_{BEP}/A_{SC_inlet}). The discretization uncertainty in the solution with the chosen mesh using the GCI method is represented by the vertical error bars, which shows a maximum of $\sim 1.8\%$ uncertainty towards the SC top wall ($z^* \rightarrow 1$); excluding the boundary layer region which shows $\sim 29\%$ uncertainty as the velocity magnitude is smaller and the relative uncertainty is thus larger.

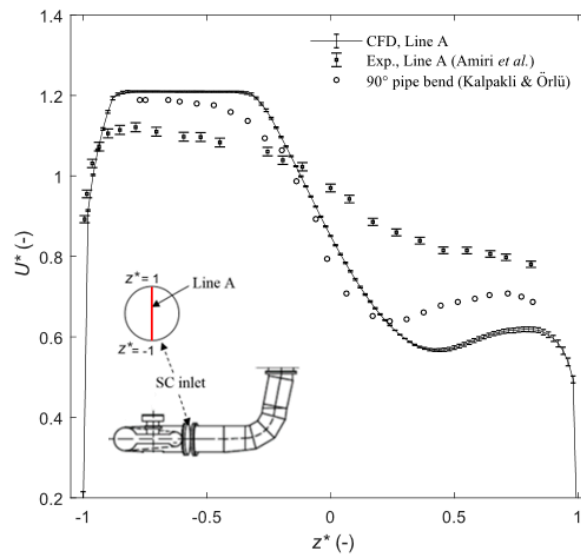


Figure 5. Normalized streamwise velocity (U^*) profile along Line A, with discretization error bars for the chosen (fine) mesh in the study. z^* is the dimensionless vertical distance in the spiral casing. The velocities are scaled by the bulk velocity (Q_{BEP}/A_{SC_inlet}). Experimental data for Line A is from Amiri et al. [26], with the error bar assumed to 1% of the value which is reasonable for LDA measurements. The data from Kalpakli and Örlü [38] is for a 90° pipe bend measured with a hot-wire.

The velocity distribution obtained from the present CFD study shows discrepancy with the measurements conducted with a two-component LDA system by Amiri et al. [26] (see Figure 5). The authors in [26] also performed numerical simulation and investigated the effects of mesh size, downstream geometries (runner and draft tube) and upstream geometry (upper tank) on the velocity distribution at the SC inlet. The simulations were conducted using scale adaptive simulation based on the SST turbulence model (SAS-SST), which is an improved URANS formulation with the capability to adapt the length scale to resolve turbulent structures—resulting in LES-like behavior in unsteady regions of the flow field. Only the inclusion of the upstream tank affected the numerical results, but no significant improvement was achieved. Therefore, the discrepancy can be attributed to either not properly modeling the upstream tank including the performance of the URANS model or the quality of the measurements itself. Nonetheless, the velocity follows a typical distribution observed in curved pipes, with larger velocity towards the outer wall and smaller velocity in the inner wall of the bend. Figure 5 also shows the velocity profile agrees well with 90° pipe bend measurements with a hot-wire from Kalpakli and Örlü [38]. This velocity distribution signifies the formation of Dean vortices [38,39].

In Figure 6, the tangential and radial velocities at two locations: S_I and S_{II} (shown in Figure 1b) are compared with the experimental results from Mulu & Cervantes [27]. The experiment was performed using a two-component LDA system with an 85 mm fiber optic probe from Dantec. Overall, the tangential velocity obtained from the CFD closely follows the experimental results. Towards the lower wall ($z^* \rightarrow -1$), the tangential velocity is smaller, and the radial velocity is larger than the experimental results. A larger magnitude of radial velocity indicates a stronger secondary flow. The magnitude of the radial velocity is small compared to the tangential velocity and subject to large variation. Therefore, an accurate comparison between the numerical and experimental results is sensible to the exact position.

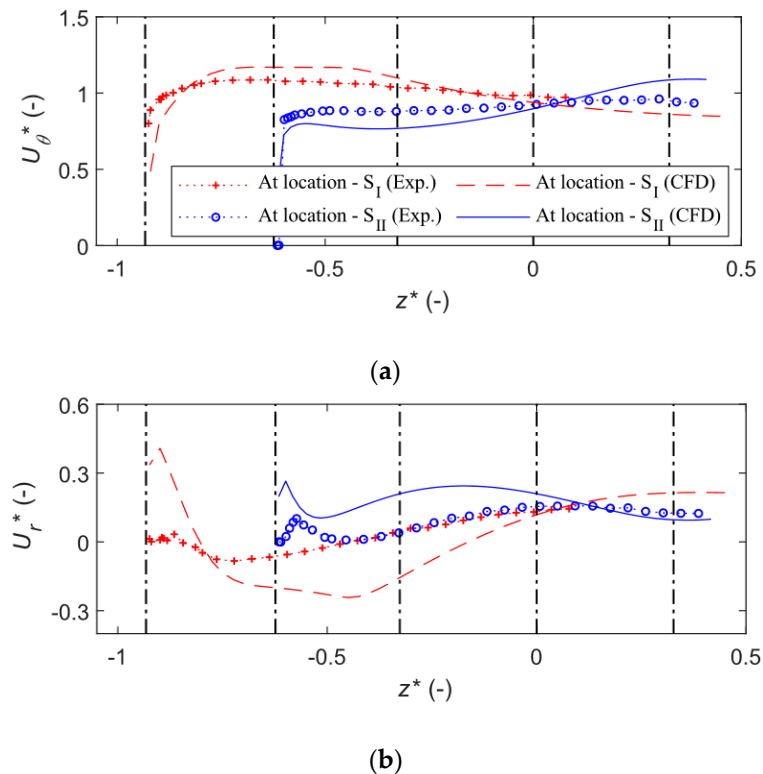


Figure 6. (a) Normalized tangential velocity (U_{θ}^*); (b) radial velocity (U_r^*) at the spiral casing (SC) measurement locations: S_I and S_{II}. The velocities are scaled by the bulk velocity U_b . The measurement locations can be found in Figure 1b. z^* is the dimensionless vertical distance in the spiral casing. The experimental data are from Mulu and Cervantes [27]. The dashed-dotted vertical lines represent, from left to right: the bottom of the SC at S_I, the bottom wall of the SC at S_{II}, the lower level of the leading of the stay vanes (SVs)/guide vanes (GVs), the mid-span of the GV, and the upper level of the leading edge of the SVs/GVs.

3. Results

3.1. Variation of Pressure Difference ΔP and Flow Rate

The variation of ΔP for the WK configurations at $\theta = 101^\circ$ during deceleration is presented in Figure 7. Two time-steps are considered in this study, as described in Section 2.4.4. ΔP drops towards zero irrespective of its value at the BEP condition. This is expected since the flow rate reduces towards zero.

The pressure difference on the upper half of the SC, ΔP_{1u} , and ΔP_{2u} , drops to zero and even becomes negative (i.e., $P_{2u} > P_{ou}$ and $P_{1u} > P_{ou}$) earlier than for the lower configurations, ΔP_{1d} and ΔP_{2d} . Although ΔP_{2u} magnitude is the second largest at BEP, it is the first one to have a negative value during the deceleration. Pressure point P_{2u} is influenced by a large pressure built up around the upper notch, i.e., a low velocity region; marked with a dashed circle in Figure 7. This behavior is similar at all other cross-sections of the SC considered in this study. No large pressure was built up around the lower notch zone, i.e., around P_{2d} . This phenomenon was not observed in the accelerating flow. Moreover, there is an asymmetry in pressure distribution on the cross-sections of the SC, see Figure 7, which is mainly caused by the upstream bent penstock.

The variation of the transient flow rate during acceleration and deceleration is presented in Figure 8a,b, respectively. The flow rates obtained at steady conditions are also shown in the figures. The steady flow rate varies almost linearly and closely follows the GVA. For an accelerating flow, the flow rate increases almost linearly at the beginning of the transient but the rate decreases towards the

end, i.e., when $t_a \cong 2.77$ s ($\alpha = 26.5^\circ$). The deviation (%) between the transient and steady flow rate was studied and calculated as:

$$Dev (\%) = 100 \times \frac{\Delta q}{Q_{BEP}}, \tag{4}$$

where Δq is a difference between the transient and steady flow rate. The maximum deviation between the transient and the steady flow rate, calculated from Equation (4), is $\sim 8\%$ when $t_a \sim 2.77$ s. The flow takes a while to reach the BEP flow conditions even after the transient movement of the GV is finished. The flow rate is slightly larger during the deceleration compared to the steady flow rates, with a maximum deviation of $\sim 4.5\%$ when $t_d \sim 1.52$ s ($\alpha = 13^\circ$).

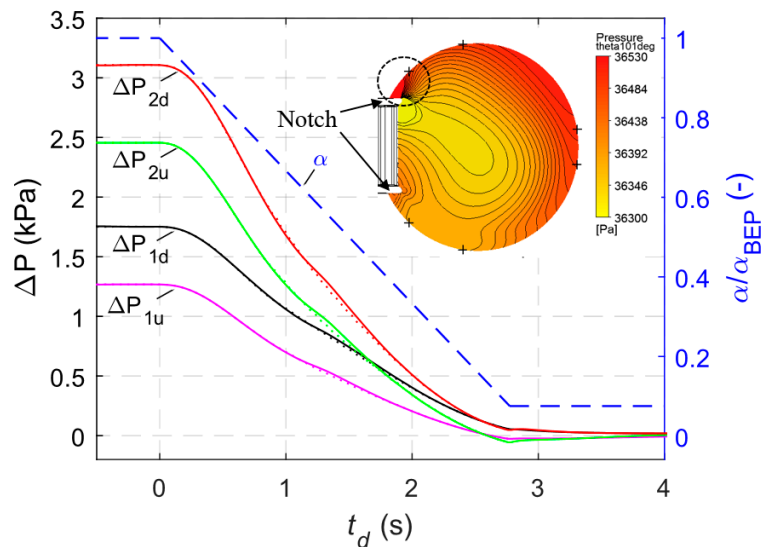


Figure 7. Variation of the pressure difference ΔP for the WK configurations at $\theta = 101^\circ$; solid continuous lines: with $\Delta t = 0.0226$ s ($\Delta\alpha = 0.2^\circ/\Delta t$), dotted lines: with $\Delta t = 0.0057$ s ($\Delta\alpha = 0.05^\circ/\Delta t$). The continuous and dashed lines overlap. The pressure contours on a cross-sectional plane of the SC at $\theta = 101^\circ$ at $t_d = 2.58$ s is also shown in the figure. The plus signs (+) marked on the figure are the locations of the pressure points. A larger pressure is built up around P_{2u} point, marked with the dashed circle, near the upper notch region.

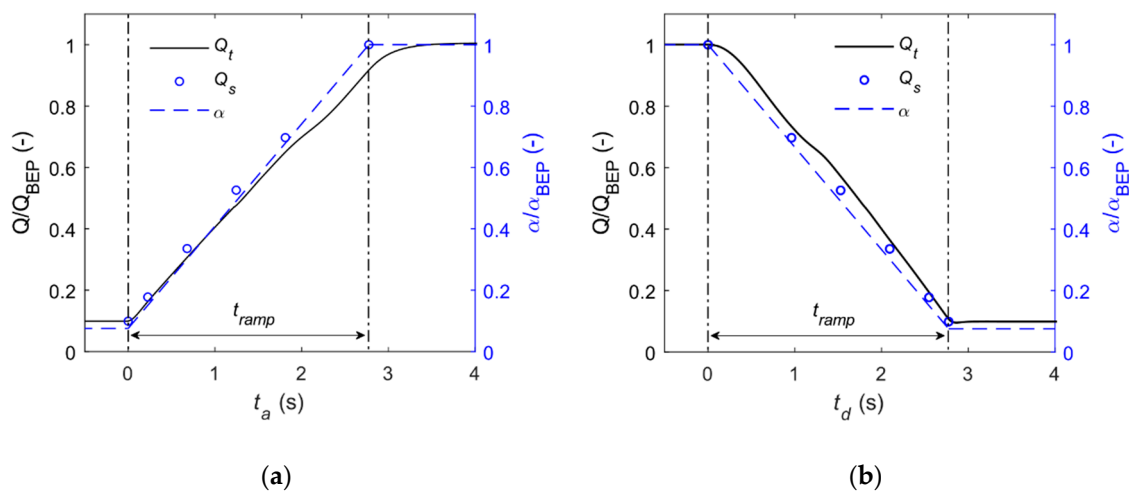


Figure 8. Flow rate variation over time, transient flow rate Q_t . (a) During an acceleration and (b) during a deceleration. The ramp time for the transient, t_{ramp} , is 2.77 s. Q_s is the steady flow rate obtained from the simulations at stationary GV angle (GVA) (α).

The flow shows some delays during the transients to reach its corresponding steady value for a given GVA, which might be attributed to the inertia of the fluid. The behavior of the flow during transient is influenced by inertia and turbulence dynamics and can be significantly different from its quasi-steady behavior, as was studied in [16,19].

As the flow rate shows a quasi-linear relationship with the GV opening (see Figure 8), it is interesting to see if the GV opening is sufficient to predict the flow rate during transients. The deviation between the flow rates with respect to the GV plotted in Figure 9. The deviation is calculated as:

$$Dev (\%) = 100 \times \left(\frac{Q}{Q_{BEP}} - \frac{\alpha}{\alpha_{BEP}} \right). \quad (5)$$

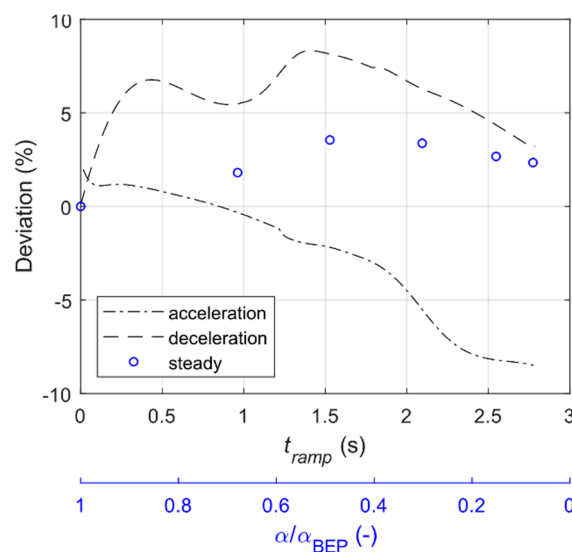


Figure 9. Deviation between the flow rates (transient and steady) and the GV opening, calculated from Equation (5).

The steady flow rate is within 3.5%, whereas the transient flow rates show a larger deviation (~8%) in both accelerating and decelerating cases. It suggests that the estimation of the transient flow rate based only on the GV opening can induce a larger error than for the steady flow rate estimation. The estimation of the transient flow rates with the WK method is presented in the coming sections.

3.2. Variations of the WK Coefficients During Transients

This section presents the behavior of the WK coefficients during transients. The instantaneous WK coefficients during deceleration are also compared to the steady WK coefficients obtained at several stationary GVAs. The instantaneous coefficients during transients were calculated from $K_{WK} = Q / \sqrt{|\Delta P|}$, where Q and ΔP are instantaneous flow rate and pressure difference, respectively during transients. The absolute value of ΔP was taken as negative values of ΔP were obtained for some WK configurations during deceleration, discussed later.

3.2.1. Decelerating Flow

The variation of the WK coefficients, K_{WKs} , in a decelerating flow at the considered azimuthal locations is presented in Figure 10. The figure also includes the steady WK coefficients obtained at several stationary GVAs. All the coefficients in the figure are scaled by the coefficients obtained at the BEP condition, K_{WK_BEP} . Therefore, the perfect WK configurations should have a value of 1.

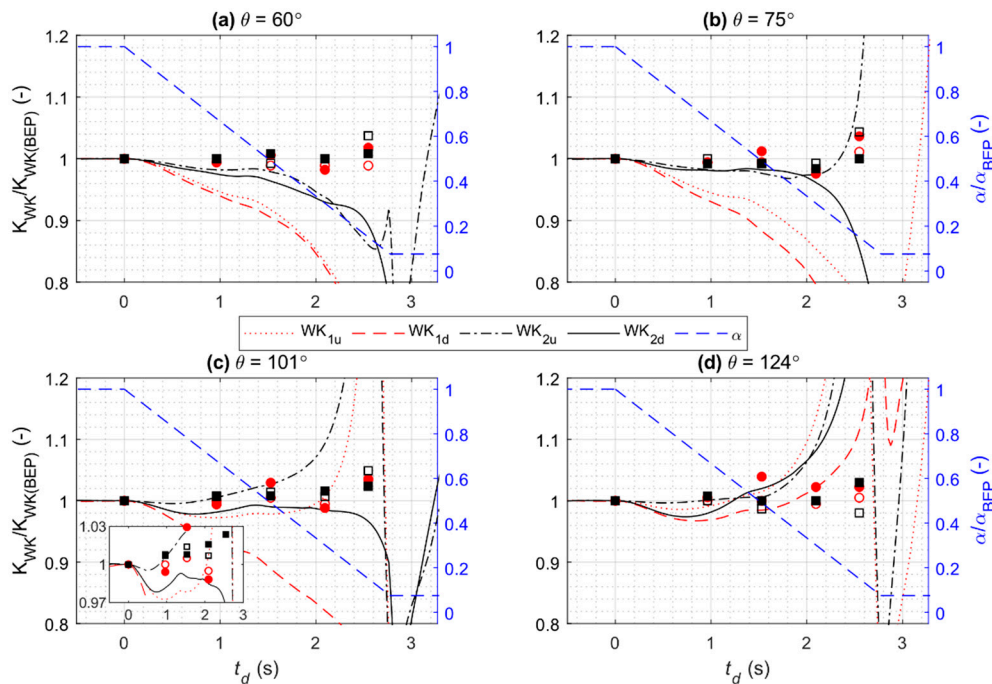


Figure 10. Variation of the WK coefficients over time during deceleration at four different azimuthal locations (θ) of the SC. Steady WK coefficients obtained at five GVAs (α) are represented by the symbols: \circ , WK1u; \bullet , WK1d; \square , WK2u, \blacksquare , WK2d. The WK coefficients were calculated from Equation (1) with $n = 0.5$ and the absolute value of ΔP , i.e., $K_{WK} = Q / \sqrt{|\Delta P|}$ —as negative values of ΔP s were observed towards the end of the deceleration. Q and ΔP are instantaneous flow rate and pressure difference, respectively during deceleration.

The sensitivity of the coefficients in the transient depends on the WK configuration and their azimuthal location in the SC. Overall, the WKs with a larger ΔP at BEP tends to be stable during the transient, see WK_{2d} in Figure 10a–c. The most stable configuration is WK_{2d} at $\theta = 101^\circ$, with a maximum deviation of about 3% from its BEP value during the transient ($t_d < 2.77$ s), however, the deviation increased over 20% immediately after the transient time, around $t_d = 3$ s. The flow rate and pressure difference have low values at the end of the deceleration (see Figures 7 and 8b) and induces a larger deviation. Moreover, the flow becomes unsteady at low flow rate regime and takes some time to reach quasi-steady stage. Therefore, the post-transient response might be neglected or treated carefully to avoid a larger deviation. WK_{2d} at $\theta = 124^\circ$ is not stable (Figure 10d) and shows similar behavior to other configurations. The figures also show WK taps can induce very large errors (>20%) in the transient flow rate measurement, which is over twice the error associated with the flow rate estimated from the GV opening, as presented in Figure 9. This shows the WK method can outperform the GV opening approach to predict the transient flow rate if the WK taps are in proper locations.

The deviations in the steady coefficients are also in a similar range, with a maximum deviation of 4.4% from their BEP values. The flow in the present type of SC, i.e., full SC, seems to be less sensitive to the GV openings compared to that observed in semi-spiral casing [40].

Towards the end of the decelerating period, negative values of ΔP , i.e., inner pressure larger than the outer pressure, were obtained for some WK configurations. The configurations showing this behavior are WK_{1u} at $\theta = 101^\circ$ and 124° , WK_{2u} at $\theta = 75^\circ$, 101° , and 124° , and WK_{2d} at $\theta = 124^\circ$. Furthermore, even after the transient time, i.e., when $t_d > 2.77$ s, the coefficients are still varying because of the flow unsteadiness in this regime.

3.2.2. Accelerating Flow

The variation of K_{WKs} in the accelerating flow is presented in Figure 11a–d. The values are scaled by the BEP values. The behavior of the coefficients is like those in the decelerating flow—WK configurations with larger ΔP tends to be more stable. However, the deviations are in a range of 10% of their BEP values. WK_{2u} configuration is more comparatively stable than the other configurations. The most stable configuration is at $\theta = 101^\circ$ and 124° , see Figure 11c,d.

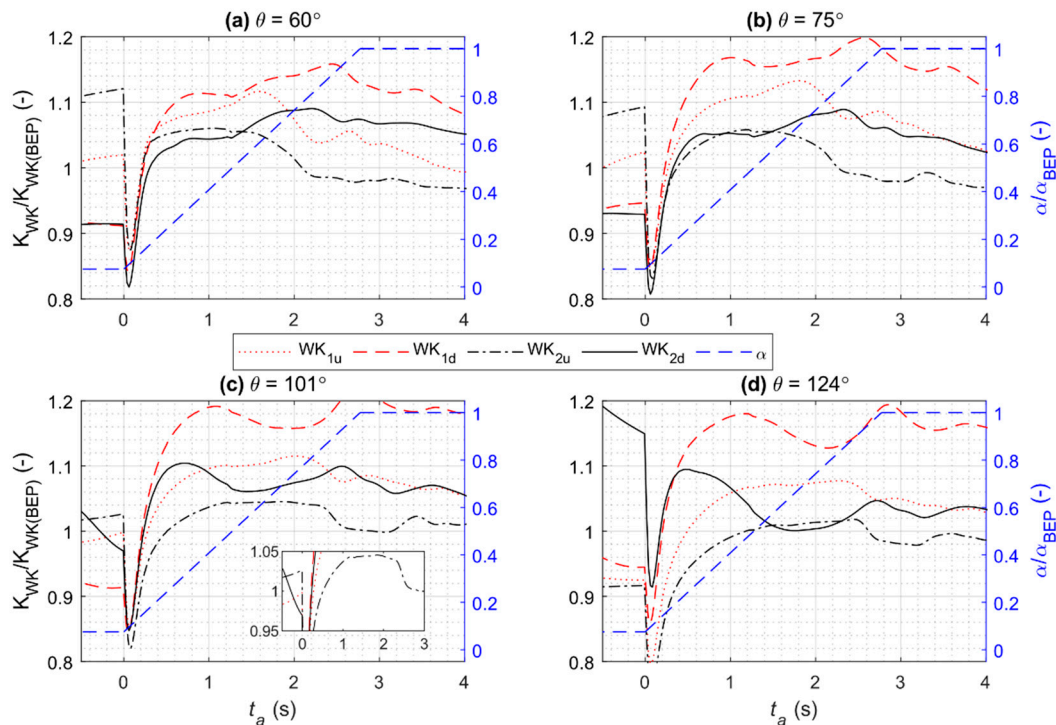


Figure 11. Variation of the WK coefficients over time during acceleration at four different azimuthal locations of the SC. The WK coefficients were calculated from Equation (1) with $n = 0.5$. The coefficients after the transient time, i.e., when $t_a > 2.77$ s do not coincide with the value of 1 because the flow takes some time after the transient to stabilize and be steady.

Immediately after the beginning of the transient, $0 \text{ s} < t_a < 0.3 \text{ s}$, the coefficient decreases abruptly and then gradually increases, see Figure 11. These dips are the results of a sudden decrease of the pressure when the GVs starts to open as the flow accelerates. When the flow rate begins to increase, the rate of velocity increment at the inner pressure point is larger than at the outer pressure points. So, the rate of ΔP increment becomes larger in the beginning. However, there is still a small delay in the flow rate to increase. Consequently, the WK coefficients show sudden dips and gradually take a steady value as the GVs open.

The coefficients are not constant, and the ratio does not have a value of 1 before the onset of the acceleration, i.e., $t_a < 0 \text{ s}$ (i.e., when $\alpha = 2^\circ$). This is due to the unsteady nature of the flow in a low flow rate regime, as mentioned before. However, no negative ΔP s were observed in accelerating flow, unlike in the decelerating flow as mentioned before. The coefficients also take some time to stabilize after the transient time, $t_a > 2.77 \text{ s}$. Ramp-up flows are observed to have a post-transient response and the flow takes some time to stabilize, see the post-transient response in ramp-up pipe flow by He and Jackson [15].

3.3. Practical Use of the WK Method in Transients

An alternative way to look at the variation of the WK coefficients during transients is by studying the variation of ΔP with Q_t , the flow rate at any instant during the transient. The WK coefficients

and exponent values are then estimated by curve fitting, usually with a power rule in Equation (1). Figure 12a and b show the variation of ΔP with Q_t in an accelerating and decelerating flow, respectively. Figure 12 is plotted on a log–log scale for better visual reference. The results are presented for the WK configurations at $\theta = 101^\circ$. The data from the curve fitting with Equation (1) are presented in Table 4. If the value of n is close to 0.5, the coefficient can be calibrated only at BEP (a single point calibration) and then used to estimate Q_t . A departure from $n = 0.5$ signifies that the coefficient changes during the transient; a single point calibration may induce a larger error. The data in Table 4 supports the results observed earlier—the most stable configurations using a single point calibration are WK_{2u} and WK_{2d} for an accelerating and a decelerating flow, respectively, as the value of n is close to 0.5.

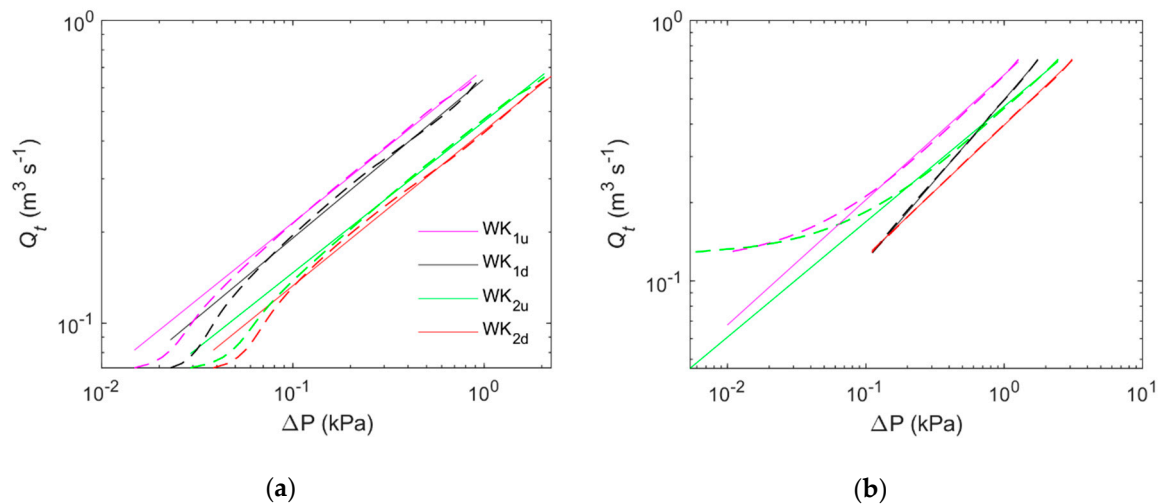


Figure 12. Evolution of the pressure difference ΔP with the flow rate during transient for four WK configurations at $\theta = 101^\circ$, shown by the dashed lines. The continuous straight lines show the curves fitted with Equation (1) and the fitted values are presented in Table 4. (a) Acceleration and (b) deceleration. The legends are provided in figure (a).

Table 4. WK coefficient K_{WK} and exponential n from curve fitting in Figure 12. R -squared (R^2) values in the table show a good fit for the data.

WK	K_{WK}		n		R^2	
	Acceleration	Deceleration	Acceleration	Deceleration	Acceleration	Deceleration
WK _{1u}	0.693	0.619	0.508	0.480	0.998	0.994
WK _{1d}	0.642	0.619	0.526	0.480	0.997	0.999
WK _{2u}	0.465	0.468	0.500	0.443	0.997	0.993
WK _{2d}	0.433	0.397	0.512	0.504	0.999	0.999

The implication of the above results is that the transient flow rate may be estimated by using the coefficient obtained at BEP and ΔP measured during the transients, such as:

$$Q_{est} = K_{WK_bep} \times \sqrt{\Delta P}, \quad (6)$$

where Q_{est} is the estimated flow rate using the WK coefficient obtained at BEP, K_{WK_bep} and ΔP is the pressure difference (instantaneous) during the transient. The deviation between Q_{est} and the transient flow rate Q_t obtained from the simulation is shown in Figure 13 for the WK configurations at $\theta = 101^\circ$, is calculated as:

$$Dev (\%) = \frac{Q_{est} - Q_t}{Q_t} \times 100. \quad (7)$$

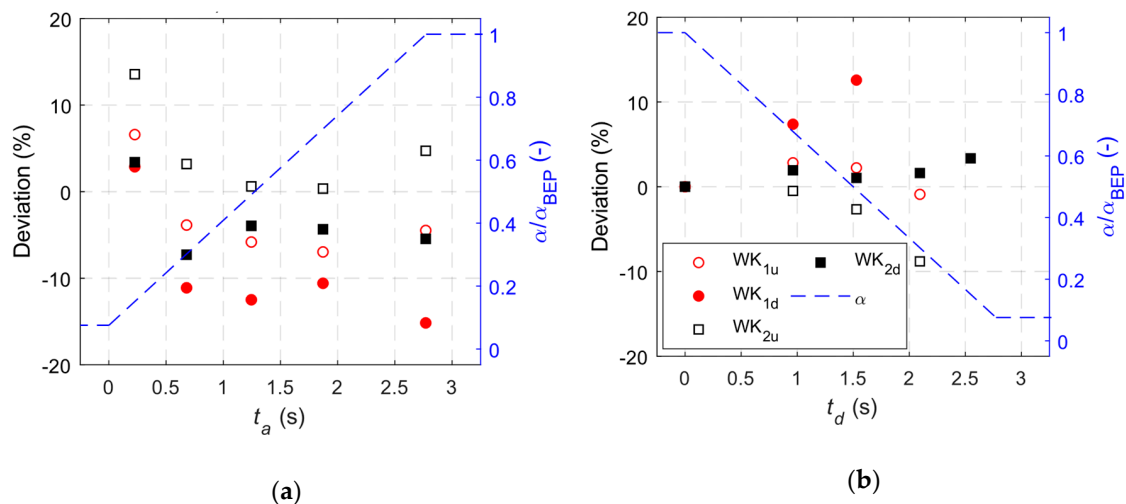


Figure 13. Deviation in the estimated flow rate and the transient flow rate obtained from the simulation with the WK configurations at $\theta = 101^\circ$, calculated using Equation (6). (a) Acceleration and (b) deceleration.

The least deviation in the flow rates is obtained with the WK_{2d} configuration, with a maximum deviation of 7.3% and 3.5% for an accelerating and decelerating flow, respectively. The deviations are lower than those estimated by the GV opening approach (see Figure 9)— suggesting a better accuracy of the WK method in transient flow estimation.

3.4. Flow Physics

The study of the flow physics inside the SC during the transients and steady conditions are presented in the following sections. This will help to understand the factors necessary to stabilize the WK coefficients.

3.4.1. Velocity and Vorticity Development

The development of the velocity along the line representing WK_{2d} during the acceleration and deceleration is shown in Figures 14a–c and 14d–f, respectively. The results are scaled by U_b , the bulk velocity. Three different cross-sections of the SC at $\theta = 0^\circ$, 60° , and 101° are considered to study the flow development in the SC. The figures show the velocity profiles are nearly preserved for all the cases. Overall, the velocity in the decelerating flow is larger than for the accelerating flow, for example at $t_a = 1.81$ s (or when $\alpha = 18^\circ$), the maximum velocity at $\theta = 0^\circ$ is only $\sim 80\%$ of U_b (Figure 14a) during the acceleration, but it is almost equal to U_b in the deceleration (see $t_d = 0.96$ s in Figure 14b). This means that the transient flow rate is larger in the decelerating flow than in the accelerating flow at a particular α , which was observed in Figure 8. The velocity profiles in the deceleration are oscillating, suggesting the presence of a larger amount of secondary flow in the region. In other words, the flow becomes more chaotic in the deceleration than in the acceleration. Furthermore, there is a flow asymmetry between the upper and lower half of the SC cross-section in the deceleration (not presented here). However, the flow during the acceleration is more symmetric between the upper and lower half of the cross-section and showed more like the vortex-flow distribution and accelerating stabilizes the flow while decelerating destabilizes.

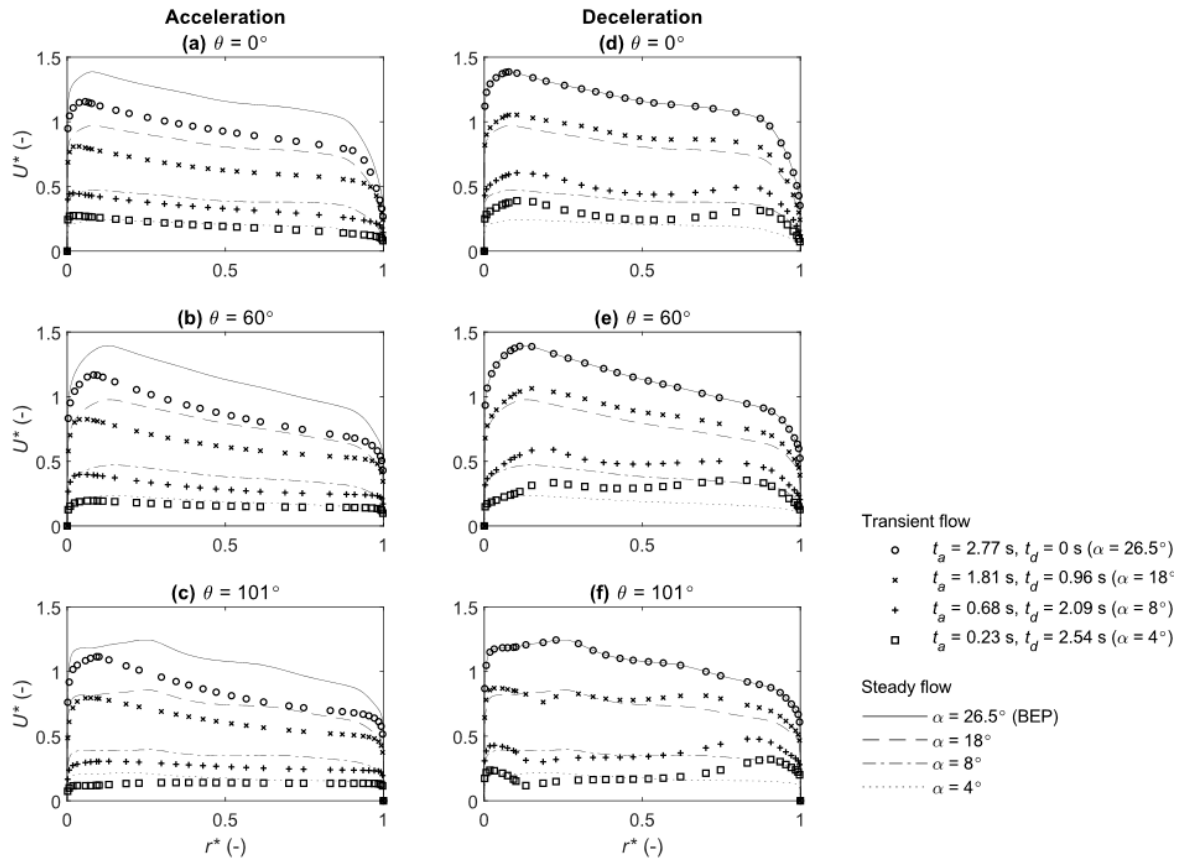


Figure 14. Development of the streamwise velocity (U^*) during an acceleration (a–c) and deceleration (d–f) along the radial distance r^* , given by $r^* = (r - r_i)/(r_o - r_i)$, where, r_i and r_o are the radial distance of the inner pressure point (P_{2d}) and outer pressure point (P_{od}). The results are plotted at three azimuthal locations of the SC for four different GVAs (including best efficiency point (BEP)) during the transients and in steady conditions.

The total vorticity represents the intensity of the secondary flow [41] and helps to understand the flow inside the SC. Figure 15 shows the normalized area-averaged vorticity, $\Omega^* = \Omega/\Omega_{max}$, where Ω is the area-averaged vorticity at a cross-sectional plane of the SC and given by:

$$\Omega = \frac{1}{A_\theta} \int_{A_\theta} \left(\frac{\partial u_z}{\partial r} - \frac{\partial u_r}{\partial z} \right) dA, \quad (8)$$

where A_θ is the area of a cross-sectional plane at angle θ .

The strength of the secondary flow increases along the azimuthal direction of the SC, at least until $\theta = 101^\circ$ for most of the cases presented in Figure 15a. The growth of the secondary flow from the inlet to about one-third of the circumference ($\theta \sim 120^\circ$) of the scroll of a radial turbine was also observed in an experimental study by Hara et al. [42]. The total vorticity at a cross-section in curved pipes is zero due to the presence of the contra-rotating Dean vortices [41]. However, in the present SC, the vortices are asymmetric and of different strengths, which are due to the combined effects of upstream bent, SC geometry and radially inward flowing conditions, see Figure 15b. Therefore, the vorticity Ω^* presented in Figure 15a is the net strength of the vortices, i.e., the difference between the counter-clockwise and clockwise vortices, where counter-clockwise vortices being stronger. The strong secondary flow also transports the low momentum fluids in the boundary layer radially inwards, Figure 15b. The magnitude of the vorticity in the acceleration is smaller than in the deceleration—signifying a lower magnitude of secondary flow in accelerating flow. It will be shown later that the secondary flow can be an important factor to balance the radial pressure gradient and make the WK coefficients stable.

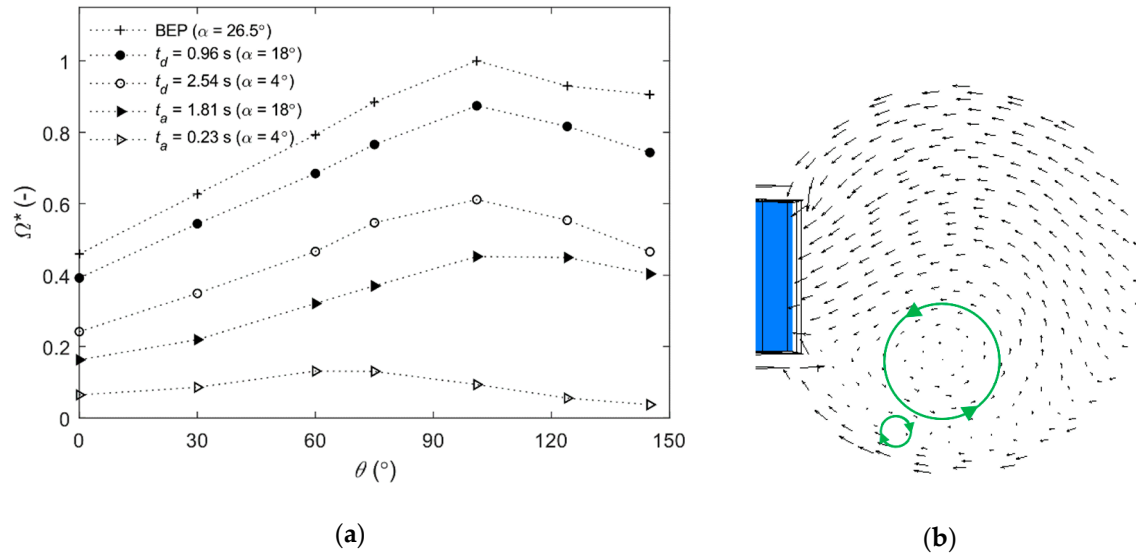


Figure 15. (a) Normalized total vorticity on the cross-sections along the SC at BEP and two time instants in acceleration and deceleration, corresponding to the same GVAs. (b) In-plane velocity vectors on $\theta = 101^\circ$ plane at BEP showing secondary flow structure; vortices are schematically shown by the circles and direction by arrowheads.

3.4.2. Turbulence, Secondary Flow, and Temporal Forces

Flow in curved pipes is characterized by a radial pressure gradient balancing the centrifugal force exerted by the fluid due to its curvilinear motion. The URANS equation in a radial coordinate are now considered to study the various forces acting on the flow during steady and transient flows. The URANS equation can be written in the differential form as:

$$\rho \frac{\partial \bar{u}_r}{\partial t} + \frac{\partial \bar{P}}{\partial r} - \rho \frac{\bar{u}_\theta^2}{r} + \rho \left[\bar{u}_z \frac{\partial \bar{u}_r}{\partial z} + \bar{u}_r \frac{\partial \bar{u}_r}{\partial r} + \frac{\bar{u}_\theta}{r} \frac{\partial \bar{u}_r}{\partial \theta} \right] - \mu \left[\nabla^2 \bar{u}_r - \frac{\bar{u}_r}{r^2} + \frac{2}{r^2} \frac{\partial \bar{u}_\theta}{\partial \theta} \right] - T_t = 0, \quad (9)$$

where ∇^2 is the Laplacian operator and T_t is the turbulence term. Following the notions presented in [43], the following terms are considered:

The radial pressure gradient (RPG): $\partial \bar{P} / \partial r$;

The centrifugal force (CF): $\rho \bar{u}_\theta^2 / r$;

The spatial inertial force (SIF): $\rho \left[\bar{u}_z \frac{\partial \bar{u}_r}{\partial z} + \bar{u}_r \frac{\partial \bar{u}_r}{\partial r} + \frac{\bar{u}_\theta}{r} \frac{\partial \bar{u}_r}{\partial \theta} \right]$;

The temporal inertial force (TIF): $\rho \partial \bar{u}_r / \partial t$;

The turbulence and viscous term (TV): $-T_t - \mu \left[\nabla^2 \bar{u}_r - \frac{\bar{u}_r}{r^2} + \frac{2}{r^2} \frac{\partial \bar{u}_\theta}{\partial \theta} \right]$.

The effect of these terms is analyzed, and the results are presented along the line representing WK_{2d} at $\theta = 101^\circ$, as it was one of the most stable WK configurations. The variations of the terms of Equation (9) are presented for steady flows in Figure 16a–c, decelerating flow in Figure 16d,f, and accelerating flow in Figure 16f,g. The steady results are presented at $\alpha = 26.5^\circ, 18^\circ$, and 8° , whereas the results for the accelerating and deceleration flows are presented at the times when $\alpha = 18^\circ$ and 8° during the transients. The magnitude of the terms M^* are scaled by the maximum value of the RPG term for a given α in the steady flow.

During the steady operation, the distribution of the terms is almost preserved, and the magnitude of the terms reduces with α ; see Figure 16a–c. At all the GVAs considered, the CF is larger than the RPG towards the inner wall ($r^* \rightarrow 0$) and outer wall ($r^* \rightarrow 1$) of the SC. Although the CF shows a smooth variation in the core region, the RPG distribution is oscillatory. The oscillatory variation of the RPG is mainly due to the SIF - secondary flow. The relative magnitude of the SIF slightly increases when $r^* \rightarrow 0$ at small α , which increases the magnitude of the RPG term.

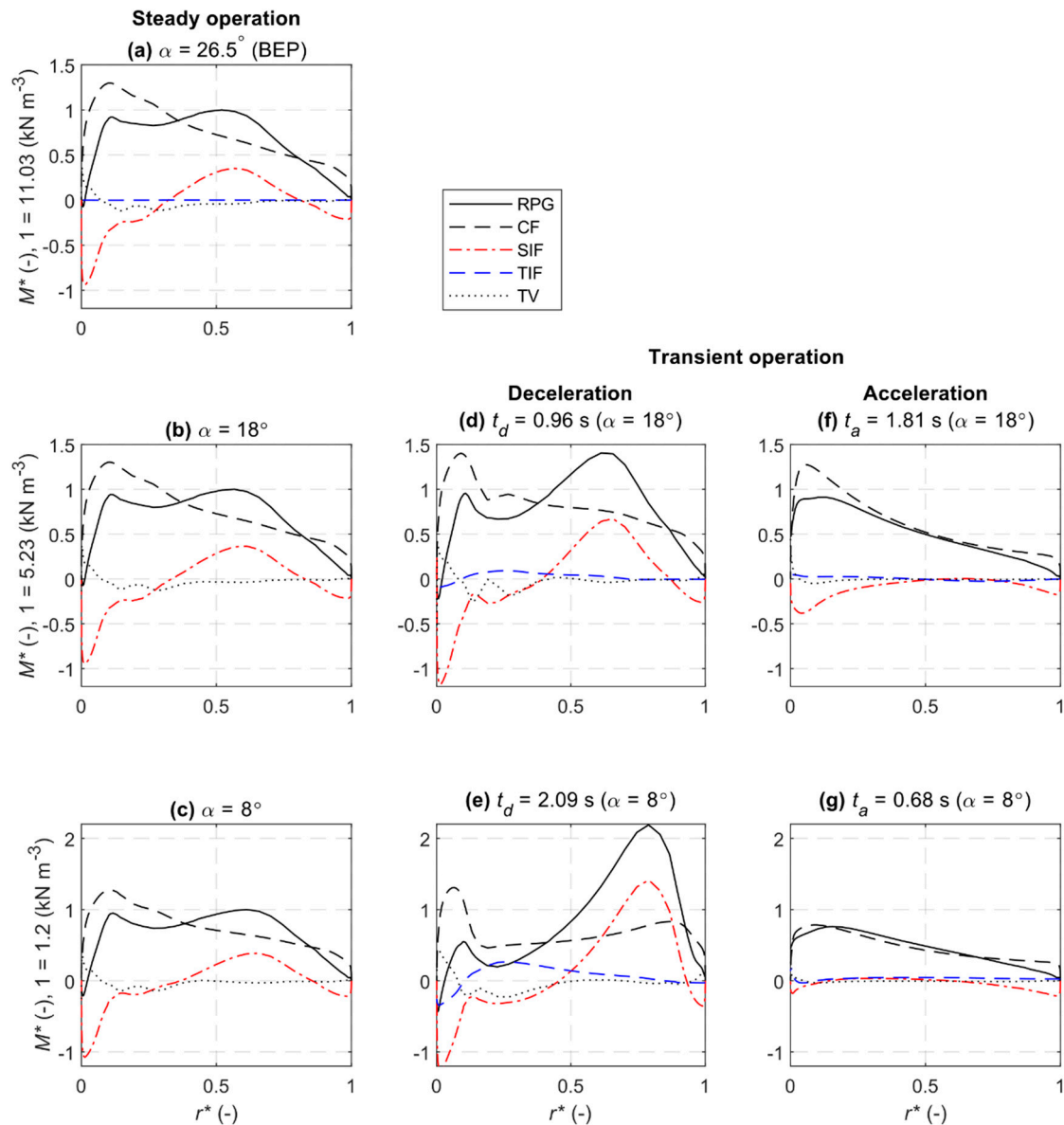


Figure 16. Variation of different terms at WK_{2d} for steady operations (a–c), deceleration (d and e) and acceleration (f and g). RPG: radial pressure gradient, CF: centrifugal force, SIF: spatial inertial force, TIF: temporal inertial force, VT: Viscous and turbulence term; see Equation (9).

During the deceleration, the distribution of the terms is still fairly preserved, at least in the early part of the deceleration; see Figure 16d,e. The SIF magnitude increases and the TIF term also become significant during the deceleration. For example, at $t_d = 0.96$ s, the TIF constitutes $\sim 7\%$ of the maximum magnitude of the RPG, whereas it increases to $\sim 26\%$ at $t_d = 2.09$ s. Although, there is a change in the magnitude of the TV and SIF affecting the distribution of the RPG term, K_{WK} was observed to be stable. This means the proper reduction rate of ΔP during the deceleration is attributed to these terms.

The values of RPG and CF are largely balanced in the case of the accelerating flow, see Figure 16f,g. This signifies the flow in the acceleration is more like the vortex flow distribution. However, K_{WKS} showed larger deviations in the acceleration than in the deceleration. The magnitudes of the terms: SIF, TIF, and TV are smaller, and change significantly compared to the corresponding steady values. A study conducted by Seddighi et al. [19] in a turbulent channel also shows a similar behavior. Flow and turbulent quantities deviate significantly from the corresponding quasi-steady values in the

case of ramp-up flow and much less in ramp-down flow. This behavior was due to the response of turbulence in transient flows.

The variations of the pressure gradients during the transients are associated with the deviations in the WK coefficients presented earlier. As seen from Figure 16, the pressure gradients along the lines are balanced by—apart from the centrifugal forces—temporal and spatial inertial forces and turbulence terms. These terms contribute to maintain the distribution of the forces and, therefore, the WK coefficients showed smaller deviations during the deceleration. This means the development of the temporal force, secondary flow, and turbulence are important factors for stabilizing the WK coefficient during the transient. However, it should be noted that the flow inside the SC strongly depends on the inflow conditions [44], so the behavior of the WK configurations might change with the inlet geometry or conditions. Therefore, it is recommended to initially perform CFD simulations to understand the behavior of the WK pressure taps before conducting measurements. The locations of the WK taps depends, of course, on their accessibility during the measurement.

4. Conclusions

The WK method may be used for transient flow rate measurement by installing the WK pressure taps in proper locations. In this numerical study, the variation of the WK coefficients was studied in two cases of the transients: accelerating and decelerating flows, which were obtained by opening and closing GVs, respectively. The deviations in the WK coefficients during the transients were studied along with the coefficients obtained at the BEP flow condition (steady flow condition).

It was shown that the sensitivity of the WK method in the transient flows depends on the type of transient: accelerating or decelerating, locations of the WK pressure taps, and their combinations. The coefficients during the deceleration were observed to be more stable than for the acceleration. The flow analysis showed that the decelerating flows exhibit a larger magnitude of secondary flow, temporal forces, and turbulence than that of accelerating flow. These forces play a significant role to balance the radial pressure gradient in the SC and make some WK configurations more stable than the others. Although the accelerating flow shows a vortex type flow distribution—the radial pressure gradient and centrifugal force largely balanced—the WK coefficients significantly deviate from their BEP values and the deviations were larger than in the case of the decelerating flow.

The transient flow rate can be estimated by using the WK coefficient obtained at the BEP flow condition and the differential pressure obtained in transients. In this study, the transient flow rate with the WK_{2d} configuration at $\theta = 101^\circ$ was estimated to ~7.5% and 3.5% deviation for accelerating and decelerating flows, respectively. The WK method showed a better performance in estimating the transient flow rates than using the GV opening flow rate estimation approach. It is recommended to conduct numerical simulations and study the sensitivities of different WK configurations before the measurements.

Author Contributions: B.B. conceptualized and developed the method, performed the numerical simulations, analyze the results, and wrote the original manuscript; J.N. and B.K.G. commented, wrote -reviewed and edited the manuscript; M.J.C. conceptualized and developed the method, commented, wrote, reviewed, and edited the manuscript. All authors have read and agreed to the published version of the manuscript.

Funding: This research was funded by Svenskt Vattenkraftcentrum, SVC (“The Swedish Hydropower Center”).

Acknowledgments: The study was performed as part of Svenskt Vattenkraftcentrum, SVC (“The Swedish Hydropower Center”). SVC was established by the Swedish Energy Agency, Energiforsk and Svenska Kraftnät with Luleå University of Technology, The Royal Institute of Technology, Chalmers University of Technology and Uppsala University (www.svc.nu).

Conflicts of Interest: The authors declare no conflict of interest.

Nomenclature

A_{SC_inlet}	inlet area of the spiral casing (SC), m ²
D	penstock diameter at the inlet of the spiral casing, m
K_{WK}	WK coefficient, m ^{3.5} /kg ^{0.5}
K_{WK_BEP}	WK coefficient obtain at BEP flow condition (steady), m ^{3.5} /kg ^{0.5}
n	WK exponent
N_1, N_2, N_3	number of mesh elements in fine, medium and coarse mesh
ΔP	pressure difference between outer and inner WK pressure points, Pa
Q	flow rate (discharge), m ³ /s
Q_{BEP}	flow rate (steady) at BEP, m ³ /s
Q_{est}	estimated flow rate using K_{WK_BEP} and ΔP , m ³ /s
Q_s	steady flow rate obtained at stationary α , m ³ /s
Q_t	transient (instantaneous) flow rate, m ³ /s
Δq	difference in the transient and steady flow rate at same α
r^*	dimensionless radial distance
t	time, s
Δt	time step, s
t_a	accelerating time (transient time), s
t_d	decelerating time (transient time), s
t_0	the time when the transient starts, s
U_b	bulk velocity calculated at the SC inlet at BEP, m ³ /s
U	streamwise velocity (total), m/s
U_θ	tangential velocity, m/s
U_r	radial velocity, m/s
y^+	dimensionless wall distance
z^*	dimensionless vertical distance in the spiral casing, m
<i>Greek Symbols</i>	
α	guide vane angle, °
$\Delta\alpha$	time step in terms of guide vane rotation angle, °
θ	circumferential location/azimuthal angle of the SC, °
ρ	density of the fluid (water), kg/m ³
Ω	total vorticity

References

1. Trivedi, C.; Gandhi, B.K.; Cervantes, M.J. Effect of transients on Francis turbine runner life: A review. *J. Hydraul. Res.* **2013**, *51*, 121–132. [[CrossRef](#)]
2. Siemonsmeier, M.; Baumanns, P.; Bracht, N.V.; Schönefeld, M.; Schönbauer, A.; Moser, A.; Dahlhaug, O.G.; Heidenreich, S. *Hydropower Providing Flexibility for a Renewable Energy System: Three European Energy Scenarios—A HydroFlex Report*; HydroFlex: Trondheim, Norway, 2018.
3. Iliev, I.; Trivedi, C.; Dahlhaug, O.G. Variable-speed operation of Francis turbines: A review of the perspectives and challenges. *Renew. Sustain. Energy Rev.* **2019**, *103*, 109–121. [[CrossRef](#)]
4. International Electrotechnical Commission. *IEC-60193 Hydraulic Turbines, Storage Pumps and Pump-Turbines—Model Acceptance Tests*; International Electrotechnical Commission: Geneva, Switzerland, 1999.
5. International Standard. *IEC 60041 Field Acceptance Tests to Determine the Hydraulic Performance of Hydraulic Turbines, Storage Pumps and Pump Turbines*; International Standard: Geneva, Switzerland, 1991.
6. ASME. *PTC-18 Performance Test Code 18: Hydraulic Turbines and Pump-Turbines*; ASME: New York, NY, USA, 2002.
7. Almquist, C.W.; Taylor, J.W.; Walsh, J.T. *Kootenay Canal Flow Rate Measurement Comparison Test Using Intake Methods*; HydroVision: Sacramento, CA, USA, 2011.
8. Taylor, J.; Proulx, G.; Lampa, J. *Turbine Flow Measurement in Intakes—A Cost-Effective Alternative to Measurement in Penstocks*; Hydro: Prague, Czech Republic, 2011.

9. Leontidis, V.; Cuvier, C.; Caignaert, G.; Dupont, P.R.O.; Fammery, S.; Nivet, P.; Dazin, A. Experimental validation of an ultrasonic flowmeter for unsteady flows. *Meas. Sci. Technol.* **2018**, *29*, 045303. [[CrossRef](#)]
10. Cheesewright, R.; Clark, C.; Hou, Y.Y. The response of Coriolis flowmeters to pulsating flows. *Flow Meas. Instrum.* **2004**, *15*, 59–67. [[CrossRef](#)]
11. Lefebvre, P.J.; Durgin, W.W. A Transient Electromagnetic Flowmeter and Calibration Facility. *J. Fluids Eng.* **1990**, *112*, 12–15. [[CrossRef](#)]
12. Fraser, R.; Coulaud, M.; Aeschlimann, V.; Lemay, J.; Deschênes, C. Method for experimental investigation of transient operation on Laval test stand for model size turbines. In *IOP Conference Series Earth and Environmental Science*; IOP: Bristol, UK, 2016; Volume 49, p. 062006. [[CrossRef](#)]
13. Trivedi, C.; Cervantes, M.J.; Gandhi, B.K.; Dahlhaug, O.G. Transient pressure measurements on a high head model Francis turbine during emergency shutdown, total load rejection, and runaway. *J. Fluids Eng.* **2014**, *136*, 121107. [[CrossRef](#)]
14. Amiri, K.; Mulu, B.; Mehrdad, R.; Cervantes, M.J. Unsteady pressure measurements on the runner of a Kaplan turbine during load acceptance and load rejection. *J. Hydraul. Res.* **2015**, *54*, 56–73. [[CrossRef](#)]
15. He, S.; Jackson, J.D. A study of turbulence under conditions of transient flow in a pipe. *J. Fluid Mech.* **2000**, *408*, 1–38. [[CrossRef](#)]
16. He, S.; Ariyaratne, C.; Vardy, A. A computational study of wall friction and turbulence dynamics in accelerating pipe flows. *Comput. Fluids* **2008**, *37*, 674–689. [[CrossRef](#)]
17. Sundstrom, J.L.R.; Cervantes, M.J. Laminar similarities between accelerating and decelerating turbulent flows. *Int. J. Heat Fluid Flow* **2018**, *71*, 13–26. [[CrossRef](#)]
18. He, S.; Seddighi, M. Turbulence in transient channel flow. *J. Fluid Mech.* **2013**, *715*, 60–102. [[CrossRef](#)]
19. Seddighi, M.; Shuisheng, H.; Orlandi, P. A Comparative Study of Turbulence in Ramp-Up and Ramp-Down Unsteady Flows. *Flow Turbul. Combust.* **2011**, *86*, 439–454. [[CrossRef](#)]
20. Gorji, A.; Seddighi, M.; Ariyaratne, C.; Vardy, A.E.; O'Donoghue, T.; Pokrajac, D.; He, S. A comparative study of turbulence models in a transient channel flow. *Comput. Fluids*. **2014**, *89*, 111–113. [[CrossRef](#)]
21. Ariyaratne, C.; He, S.; Vardy, A.E. Wall friction and turbulence dynamics in decelerating pipe flows. *J. Hydraul. Res.* **2010**, *48*, 810–821. [[CrossRef](#)]
22. Winter, I.A.; Kennedy, A.M. Improved type of flow meter for hydraulic turbines. *ASCE Proc.* **1933**, *59*, 4.
23. Isaksson, H.; Sendelius, M.; Cervantes, M.J. Cam curve in Kaplan turbine, a sensitivity analysis. *UPB Sci. Bull. Ser. D* **2016**, *78*, 185–192.
24. Lövgren, M.H.; Andersson, U.; André, G. *Skew Inlet Flow in a Model Turbine—Effects on Winter–Kennedy Measurements*; Hydro: Ljubljana, Slovenia, 2008.
25. Baidar, B.; Nicolle, J.; Gandhi, B.K.; Cervantes, M.J. Numerical study of the Winter–Kennedy method for relative transient flow rate measurement. In *IAHR International Workshop on Cavitation and Dynamic Problems in Hydraulic Machinery and Systems, Stuttgart*; IOP Conference Series Earth and Environmental Science; IOP Publishing: Bristol, UK, 2019; Volume 405, p. 012022. [[CrossRef](#)]
26. Amiri, K.; Mulu, B.; Raisee, M.; Cervantes, M.J. Effects of upstream flow conditions on runner pressure fluctuations. *J. Appl. Fluid Mech.* **2017**, *10*, 1045–1059. [[CrossRef](#)]
27. Mulu, B.G.; Cervantes, M.J. LDA measurements in a Kaplan spiral casing model. In *13th Symposium on Transport Phenomena and Dynamics of Rotating Machinery*; Curran Associates, Inc.: Honolulu, HI, USA, 2010.
28. Mössinger, P.; Jester-Zürker, R.; Jung, A. Francis-99: Transient CFD simulation of load changes and turbine shutdown in a model sized high-head Francis turbine. In *IOP Conference Series: Journal of Physics*; IOP Publishing: Bristol, UK, 2017; Volume 782, p. 012001. [[CrossRef](#)]
29. Nicolle, J.; Morissette, J.F.; Giroux, A.M. Transient CFD simulation of a Francis turbine startup. In *IOP Conference Series: Earth and Environmental Science*; IOP Publishing: Bristol, UK, 2012; Volume 15, p. 062014. [[CrossRef](#)]
30. ANSYS, Inc. *CFX—Solver Theory Guide 19.1*; ANSYS, Inc.: Canonsburg, PA, USA, 2019.
31. Menter, F. Two-Equation Eddy-Viscosity Turbulence Models for Engineering Applications. *AIAA J.* **1994**, *32*, 1598–1605. [[CrossRef](#)]
32. Mössinger, P.; Zürker-Jester, R.; Jung, A. Investigation of different simulation approaches on a high-head Francis turbine and comparison with model test data: Francis-99. *J. Phys. IOP Conf. Ser.* **2015**, *579*, 012005. [[CrossRef](#)]

33. Chen, H.; Zhou, D.; Zheng, Y.; Jiang, S.; Yu, A.; Guo, Y. Load rejection transient process simulation of a Kaplan turbine model by co-adjusting guide vanes and runner blades. *Energies* **2018**, *11*, 3354. [[CrossRef](#)]
34. Trivedi, C.; Cervantes, M.J.; Dahlhaug, O.G. Numerical Techniques Applied to Hydraulic Turbines: A Perspective Review. *Appl. Mech. Rev.* **2016**, *68*, 010802. [[CrossRef](#)]
35. Saemi, S.; Raisee, M.; Cervantes, M.J.; Nourbakhsh, A. Numerical investigation of the Pressure-Time Method considering pipe with variable cross section. *J. Fluids Eng.* **2018**, *140*, 101401. [[CrossRef](#)]
36. Saemi, S.; Cervantes, M.J.; Raisee, M.; Nourbakhsh, A. Numerical investigation of the Pressure-time method. *Flow Meas. Instrum.* **2017**, *55*, 44–58. [[CrossRef](#)]
37. Celik, I.; Ghia, U.; Roache, P.; Freitas, C.; Coleman, H.; Raad, P. Procedure for Estimation and Reporting of Uncertainty due to Discretization in CFD Applications. *J. Fluids Eng.* **2008**, *130*, 078001–(1–4). [[CrossRef](#)]
38. Kalpakli, A.; Örlü, R. Turbulent pipe flow downstream a 90° pipe bend with and without superimposed swirl. *Int. J. Heat Fluid Flow* **2013**, *41*, 103–111. [[CrossRef](#)]
39. Vester, A.K.; Örlü, R.; Alfredsson, H. Turbulent Flows in Curved Pipes: Recent Advances in Experiments and Simulations. *Appl. Mech. Rev.* **2016**, *68*, 050802. [[CrossRef](#)]
40. Baidar, B.; Nicolle, J.; Gandhi, B.K.; Cervantes, M.J. Sensitivity of the Winter–Kennedy method to different guide vane openings on an axial machine. *Flow Meas. Instrum.* **2019**, *68*, 101585. [[CrossRef](#)]
41. Cuming, H.G. *The Secondary Flow in Curved Pipes*; Aeronautical Research Council: London, UK, 1955.
42. Hara, K.; Furukawa, M.; Inoue, M. Behavior of three-dimensional boundary layers in a radial inflow turbine scroll. In *ASME 1993 International Gas Turbine and Aeroengine Congress and Exposition*; American Society of Mechanical Engineers Digital Collection: Cincinnati, OH, USA, 1993.
43. Boiron, O.; Valérie, D.; Pelissier, R. Experimental and numerical studies on the starting effect on the secondary flow in a bend. *J. Fluid Mech.* **2007**, *574*, 109–129. [[CrossRef](#)]
44. Baidar, B.; Nicolle, J.; Trivedi, C.; Cervantes, M.J. Numerical Study of the Winter–Kennedy Method—A Sensitivity Analysis. *J. Fluids Eng.* **2018**, *140*, 051103. [[CrossRef](#)]



© 2020 by the authors. Licensee MDPI, Basel, Switzerland. This article is an open access article distributed under the terms and conditions of the Creative Commons Attribution (CC BY) license (<http://creativecommons.org/licenses/by/4.0/>).